IOPscience iopscience.iop.org

Home Search Collections Journals About Contact us My IOPscience

A kinetic Monte Carlo study on the role of defects and detachment in the formation and growth of In chains on Si(100)

This article has been downloaded from IOPscience. Please scroll down to see the full text article.

2009 J. Phys.: Condens. Matter 21 405002

(http://iopscience.iop.org/0953-8984/21/40/405002)

View the table of contents for this issue, or go to the journal homepage for more

Download details:
IP Address: 129.252.86.83
The article was downloaded on 30/05/2010 at 05:31

Please note that terms and conditions apply.

IOP Publishing Journal of Physics: Condensed Matter

J. Phys.: Condens. Matter **21** (2009) 405002 (8pp) doi:10.1088/0953-8984/21/40/405002

A kinetic Monte Carlo study on the role of defects and detachment in the formation and growth of In chains on Si(100)

Marvin A Albao[1,2], **J W Evans**[3,4] **and Feng-Chuan Chuang**[1,5]

[1] Department of Physics, National Sun Yat-Sen University, Kaohsiung, 804, Taiwan
[2] Institute of Mathematical Sciences and Physics, University of the Philippines Los Banos, 4031, Philippines
[3] Ames Laboratory-USDOE, Iowa State University, Ames, IA 50011, USA
[4] Department of Mathematics, Iowa State University, Ames, IA 50011, USA

E-mail: fchuang@mail.nsysu.edu.tw

Received 6 April 2009, in final form 24 July 2009
Published 8 September 2009
Online at stacks.iop.org/JPhysCM/21/405002

Abstract

Deposition on a Si(100) surface and subsequent self-assembly of In atoms into one-dimensional (1D) atomic chains at room temperature is investigated via kinetic Monte Carlo simulation of a suitable atomistic model. Model development is guided by recent experimental observations in which 1D In chains nucleate effectively exclusively at C-type defects, although In atoms can detach from chains. We find that a monotonically decreasing form of the scaled island size distribution (ISD) is consistent with a high defect density which facilitates persistent chain nucleation even at relatively high coverages. The predominance of heterogeneous nucleation may be attributed to several factors including low surface diffusion barriers, a high defect density, and relatively weak In–In binding.

(Some figures in this article are in colour only in the electronic version)

1. Introduction

It has become increasingly important to understand the mechanisms that govern the self-assembly of single-atom wide and tall atomic chains grown via deposition of group III and IV metals on Si(100) because of their potential utility in applications ranging from contacts in switches to quantum computers. Images obtained from scanning tunneling microscopy (STM) presented in previous studies [1–4] offered a detailed view of the process of self-assembly, as well as of the spatial and length distributions of the atomic chains. Complementing these experimental studies are electronic structure calculations, the goal of which is to provide information on preferential binding sites, diffusion pathways and energetics, as well as stabilities of candidate configurations for the atomic chain [5–7]. These calculations shed light on the experimentally observed development of dimerized chains of atoms with the islands aligned along the direction perpendicular to the Si dimer rows. The growth mechanisms has been described as a surface polymerization reaction. This detailed insight into island formation and the growth process (together with the feature that atoms do not populate higher layers at submonolayer coverages) makes it relatively easy to model.

Although analyses of atomic chain formation and structure on Si(100) have been performed for In [1–4, 8], Ga [4, 9, 10], and Al [5, 11], the influence of surface defects on nucleation and its consequences on the length distribution has not been fully explored. In our previous study for Ga, we attempted to assess how defect nucleation impacts on estimates of terrace diffusion barriers [10]. Recently, Kocan *et al* [12, 13] showed via real-time STM imaging techniques that In islands or chains nucleate effectively exclusively at defect sites, specifically so-called C-defects, where one end of the atomic chain is attached to the C-defect. A separate work utilizing *ab initio* calculations in [14] elucidated the strength of the attractions between defects and In monomers. In addition, the STM studies provided extraordinarily detailed information into the limited stability of the chains, determining the dependence on chain length of the rates at which In atoms detach (from the end furthest from the C-defect).

[5] Author to whom any correspondence should be addressed.

 © 2009 IOP Publishing Ltd Printed in the UK

The above extensive information guides the development of a lattice-gas model realistic enough to describe the behavior of key quantities such as mean island or chain size and density, as well as the effect of density of C-defects on these quantities. Additionally, following our recent work [9, 10] in which we argued that the monotonically decreasing form of the scaled island size distribution observed for Ga can in fact be explained naturally via restricted aggregation (relative to nucleation), it would be interesting to determine if this picture holds true even in the presence of C-defects. In the case of Ga, we also identified factors controlling the relative propensity of homogeneous versus heterogeneous nucleation.

In the current paper, in section 2, we first present results from a DFT analysis of binding sites and diffusion barriers for the In on an Si(100) system. In section 3, we then present an atomistic model for In chain formation during deposition of In on Si(100) which incorporates the above DFT results for terrace diffusion, heterogeneous nucleation at defects, as well as reversible attachment from chains based on the STM data described above. Detailed simulation results for this model are provided in section 4, together with a discussion of the behavior determined from the simulations. It should be noted that preliminary results have been reported recently for atomistic modeling of In chain formation on Si(100) [15]. This modeling of chain formation via heterogeneous nucleation incorporates reversibility, albeit with a single detachment barrier (in contrast to our more complex and realistic treatment with multiple detachment rates). Furthermore, this paper estimated diffusion barriers solely by comparison of modeling predictions with experiment. In contrast, we perform extensive DFT analysis to determine these quantities, yielding significantly different values which are incorporated into our modeling. Finally, conclusions from our study are presented in section 5.

2. DFT calculations: methodology and results

There exist previous *ab initio* studies on adsorption of group III and group V metals on Si(100) identifying binding sites and diffusion barriers for adatoms and ad-dimers [5, 7, 16]. However, none of these studies have obtained the activation barriers for surface diffusion of In on Si(100), which constitute a key input to our modeling. Here, we utilize density functional theory (DFT) analysis to identify possible pathways for diffusion along the two principal directions, and then to calculate the associated effective activation barrier for each direction. Thus, a brief description of these calculations is in order.

Our calculations were carried out within the generalized gradient approximation as parameterized by Perdew, Burke, and Ernzerhof (PBE) [17] to density functional theory [18] using projector-augmented-wave potentials [19], as implemented in the *Vienna ab initio simulation package* [20]. To simulate atomic adsorption, we used a repeated slab structure consisting of six Si layers with 12 Å vacuum. Also, we used the 4×4 supercell as the slab substrate and manipulated the $c(4 \times 2)$ at the reconstruction layer. The 2×2 Monkhorst–Pack grid was employed to sample the surface Brillouin-zone (BZ). The kinetic energy cutoff was set to 250 eV (18.37 Ryd). Additionally, the Si atoms at the bottom of the slab are passivated with hydrogen atoms, which are then kept fixed to simulate the bulk structure. The rest of the Si atoms and In atoms are allowed to relax until the residual force on each movable atom is less than 0.01 eV Å^{-1}. Similar settings were used in our previous study [21].

To map the potential energy surface (PES), we applied a similar methodology described in [16, 22]: an In atom is placed with fixed lateral position above the $c(4 \times 2)$ surface and relaxed vertically. In this way, binding energies are mapped out over a uniform grid with a spacing of 0.48 Å. Examination of the resulting PES map revealed key information such as preferential binding sites and diffusion pathways, as well as the height of the barriers for diffusive hopping between local minima. It should be noted that similar calculations for group III metals have been performed previously [7], though the activation barriers for terrace diffusion, so crucial to our modeling, have not been calculated. Note that our calculation produces a surface with buckled Si dimers, i.e. each dimer has a higher (up) and lower (down) atom. Like atoms are adjacent across dimer rows and unlike atoms are adjacent within a dimer row. See figures 1(a) and (b).

Mirroring the results for Al described in [7], we also found an off-center binding site, called the M site, where an In atom is bound to two Si atoms, as the site with the lowest energy. Our analysis suggests that diffusion along the [110] direction, perpendicular to the Si dimer row, probably proceeds via a sequence of two distinct hops: M-p-M for hops across a dimer row, and M-h-M for hops between two dimer rows; see figure 1(c). The barrier for the former is 0.27 eV and for the latter is 0.18 eV. Similarly, we identified two distinct adatom hops and corresponding activation barriers along the $[1\bar{1}0]$, parallel to the Si dimer row. These are: M-ucu-M (0.20 eV) and M-b-M (0.27 eV). Since both types of hops are required for long-range diffusion in either direction, the effective barrier is quite accurately determined by the higher of the two barriers in each direction, and is thus 0.27 eV for both directions. (This choice is confirmed by a more precise analysis[6].) For comparison, Brocks *et al* in [5] obtained 0.1 and 0.3 eV as the effective barriers for Al diffusion on Si(100) along the [110] and $[1\bar{1}0]$ directions, respectively. As a final caution, we note that higher-level embedded-cluster quantum chemistry calculations could potentially predict different preferred adsorption sites and barriers than the above DFT analysis [11].

3. Atomistic lattice-gas model for In deposition on Si(100)

3.1. Model details

In our atomistic lattice-gas modeling, the Si(100) substrate is described as a periodic rectangular array of adsorption sites

[6] Analysis of effective rates or barriers for single particle diffusion on a linear lattice with alternating rates or barriers between sites comes from consideration of the associated master equations. If h_- and h_+ are the distinct hop rates, and a is the lattice constant, then the diffusion coefficient is given by $D = 2a^2h_+h_-/(h_+ + h_-)$ correctly producing $D = a^2h$ for $h_+ = h_- = h$.

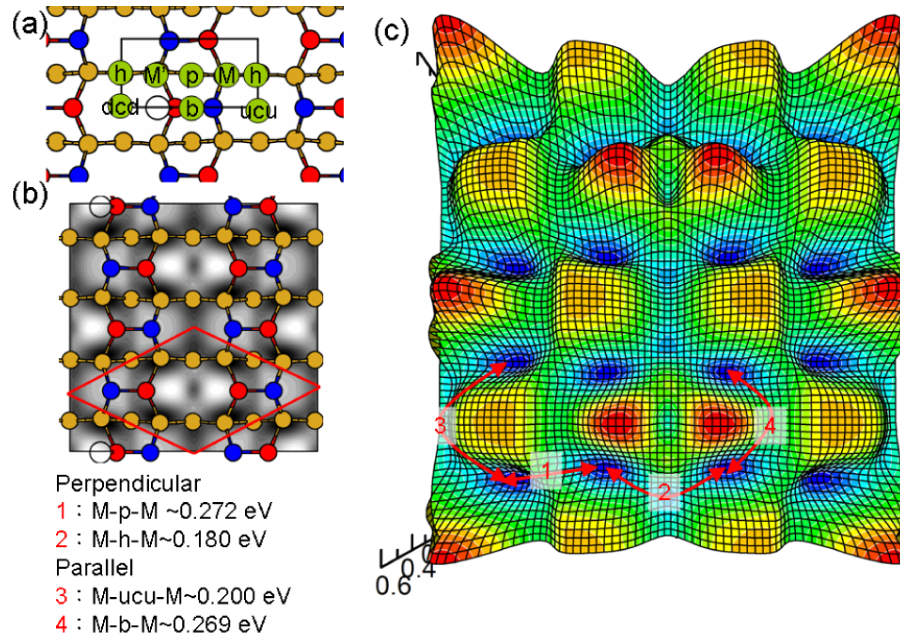

Figure 1. PES map showing possible In adsorption sites and diffusion pathways on Si(100). Dark gray (blue) and black (red) atoms indicate up and down Si atoms in dimers, respectively. Sites in the figure are labeled descriptively by b for bridge; p for pedestal; h for hollow; and c for cave, while M represents the lowest energy absorption sites. dcd denotes the cave site between two down atoms of the dimers, and ucu stands for the cave sites between two up atoms of the dimers. The c(4×2) supercell is outlined by solid lines. The paths taken by In when hopping from an M site to an equivalent neighboring M site are identified. Paths 1 and 2 are perpendicular to the Si dimer row while paths 3 and 4 run parallel to the Si dimer rows.

for In. These sites are known to correspond to locations in the trenches between Si dimer rows [7]. The dimer row reconstruction for Si(100) breaks the symmetry between orthogonal directions on this array. For convenience, we identify the Si dimer row direction as vertical, and thus the In atomic chain direction as horizontal, relative to this array. Some fraction of these adsorption sites will be designated as defects at the outset of the simulation. They are randomly distributed, subject to the constraint that adjacent defects are excluded. A more detailed prescription of the treatment of defects is provided below.

(a) Adsorption and diffusion. Indium atoms are deposited onto the array of adsorption sites at the flux rate F, typically of the order of 10^{-2}–10^{-4} atoms per site per second, i.e. monolayers (ML) per second, or ML s^{-1}. Terrace diffusion of isolated adatoms occurs along the two principal directions of the adsorption site array (i.e. perpendicular and parallel to the underlying Si dimer rows), at rates governed by the Arrhenius law, $h_{\perp,\parallel} = \nu \exp[E_{\perp,\parallel}/(kT)]$, where ν is the prefactor, typically 10^{13} s^{-1}, k is the Boltzmann constant, and T is the temperature. Diffusion barriers of $(E_{\perp}, E_{\parallel}) =$ (0.27 eV, 0.27 eV), are chosen based on the DFT analysis and subsequent discussion in section 2. Moreover, we will exclude diffusion of adatoms to 'forbidden sites' directly above and below the In atomic wires. See further discussion below.

(b) Island nucleation and growth. First, we describe further the parallel dimer picture of atomic chain or island formation on Si(100), which applies in most group III and IV metals: two adatoms which reach horizontally adjacent sites (located in the same trench in between two Si dimer rows) can dimerize to homogeneously nucleate an island or chain [7]. Subsequent growth is strictly one-dimensional and occurs along the ad-dimer axis, i.e. perpendicular to the Si dimer row. Such growth is mediated by adatom diffusion to sites at the end of the chain, recalling that sites above and below it are 'forbidden'. The existence of such 'forbidden' sites also leads to the well-known property of chains wherein no two islands can be laterally adjacent (i.e. the minimum lateral spacing between islands is two vertical lattice constants)[7]. In the current modeling, both the initial homogeneous nucleation step and subsequent chain growth are reversible (see below).

However, in the case of In/Si(100), island formation appears to be initiated primarily when a single mobile adatom is captured by a C-type defect to which it binds reversibly [12, 14]. In this scenario, initial island growth occurs when a second diffusing adatom reaches a site adjacent to a defect-bound monomer and then dimerizes to form a defect-bound dimer. Further growth proceeds by additional diffusing adatoms reaching the 'free' end of an island, i.e. the end not bound to a defect. In the current modeling, both the initial heterogeneous nucleation atoms trapping at the defect and subsequent chain growth are reversible (see below). Thus, In islands are primarily nucleated heterogeneously, rather than homogeneously, although in our modeling both pathways are operative.

(c) Reversible detachment of adatoms from defects and chain ends. In our modeling for heterogeneous nucleation, a single adatom bound at a defect can detach as noted above. For homogeneous nucleation, the initial dimer can also dissociate

[7] There is evidence in [14] that In atoms may adsorb on sites laterally adjacent to In atomic chains. However, such atoms do not nucleate islands.

Table 1. Rates for detachment of end atoms in heterogeneously nucleated islands as identified in [12] (first four entries), and their counterparts in homogeneously nucleated islands (last three entries).

Type	End atom detachment rate (s^{-1})
Defect-bound monomer	20
Defect-bound dimer	0.01
Odd-sized defect-bound island	3.7
Even-sized defect-bound island	0.2
Dimer	0.2
Monomer-terminated island	3.7
Dimer-terminated island	0.2

by detachment of either atom; see table 1 for the rates used in our simulations which were adopted from or motivated by [12].

For heterogeneously nucleated chains of more than one atom, the atom at the 'free' end (i.e. the end not pinned at a defect) will be allowed to detach at a rate depending on the island size. Such atoms are classified into three distinct types (an atom in a dimer, an atom at the end of an chain of odd length three or more, an atom at the end of a chain of even length with multiple dimers) and detachment rates assigned in accordance with the findings in [12]. We have adopted their reported values for the purpose of this simulation, as presented in table 1. Likewise, for homogeneously nucleated islands, in which there are now two 'free' ends, end atoms detach at rates which similarly depend on the island size. We take the view that the detachment rate should be the same as for their defect-bound counterparts. We argue that at the free ends of larger heterogeneously nucleated chains, the effect of a defect should be negligible. Associated rates for detachment from homogeneously nucleated islands are also listed in table 1.

(d) KMC simulation algorithm. Our KMC simulations use a refined Bortz–Kalos–Lebowitz (BKL) type algorithm [23] in which the main task is to create a dynamically updated list of possible processes (and of the adatoms associated with them), grouped by processes with the same (or similar) rates. The efficiency of such an algorithm derives from its being nearly 'rejection free'. Processes are chosen at random weighted by their rate, and one process is implemented in most time steps. Some rejection occurs if one group proceeds with a slightly different rate (in which case a successful move is determined with a probability determined by the ratio of the actual to the maximum rate for events in that group), and when an attempt to hop would move an atom to a 'forbidden' site.

3.2. Variants of the model

In this subsection to motivate our selection of model variants, we first describe two types of deposition and STM imaging procedures employed in the In/Si(100) experiments. One involves post-deposition STM imaging in which data are gathered after some desired adatom coverage has been reached by relatively fast deposition at a rate of 10^{-3}–10^{-2} ML s^{-1} [13]. Thus, the duration of the deposition phase of the experiment is short, and the defect density is effectively constant during deposition. Rapid deposition also produces far-from equilibrium island distributions, and the data obtained subsequently can be affected by some post-deposition equilibration dynamics or relaxation. The other method involves real-time STM imaging during deposition with a significantly greater separation between the evaporator and the sample. This results in a low deposition rate of around 10^{-4} ML s^{-1}, an order of magnitude slower than above. In this case, the defect density generally increases significantly during deposition.

Our simulation study takes into account these two different scenarios by introducing two variants of the model. In one the defect density is fixed at the beginning of the simulation and remains constant, and in the other the number of defects may rise during deposition.

4. Results and discussions

4.1. Morphology of In adlayers

The evolution of simulated surface morphologies of In adlayers formed by deposition of various coverages, θ, is shown in figure 2. The flux is moderately high and set to 2×10^{-3} ML s^{-1} while defect density is 0.01/site, typical of the post-deposition STM experiments described in [12, 13]. The adlayers consist of arrays of 1D islands (black atoms) pinned at C-defects (indicated by unfilled red circles). Notice that homogeneously nucleated islands, i.e. those not anchored on defects, are absent in these figures. Further analysis reveals that this feature reflects a combination of a high defect density (favoring heterogeneously nucleated islands), and a relatively high ratio of diffusion to deposition rate (despite the higher flux).

4.2. Effect of defect density on mean island size and density

In our simulations for rapid deposition at higher flux, the number of defects is fixed at its initial value, mimicking experiments with post-deposition STM imaging in [8, 13]. Specifically, we assigned high flux within the range of 10^{-3}–10^{-2} ML s^{-1} and defect densities varying from 0.0035/site to 0.01/site to reflect various experimental conditions. In one simulation run shown in figure 3 (filled red circle), where $F = 2 \times 10^{-3}$ ML s^{-1} and defect density $N_{def} = 0.01$/site, the plot reveals that after a brief initial transient period, the average island size, S_{av}, increases linearly with coverage or time. This corresponds to an initial burst of nucleation followed by growth with no further nucleation. Thus, the mean island or chain size (measured in atoms) satisfies $S_{av} = \theta/N_{av} \approx \theta/N_{def}$. This behavior is illustrated in figure 4, where we used the same flux as above, while the defect density was varied. To demonstrate that simulation behavior is generally consistent with that observed in experiments we have also provided the experimental data given in [13] (unfilled red circles).

To further test the robustness of the model and the accuracy of the parameters used, we compare simulation predictions (filled black squares) showing the dependence of mean island size on coverage with a different set of post-deposition STM imaging data obtained from [8] (unfilled black squares). In that experiment, $F = 10^{-3}$ ML s^{-1} and $N_{def} = 0.003$/site. Using the same flux rate as in

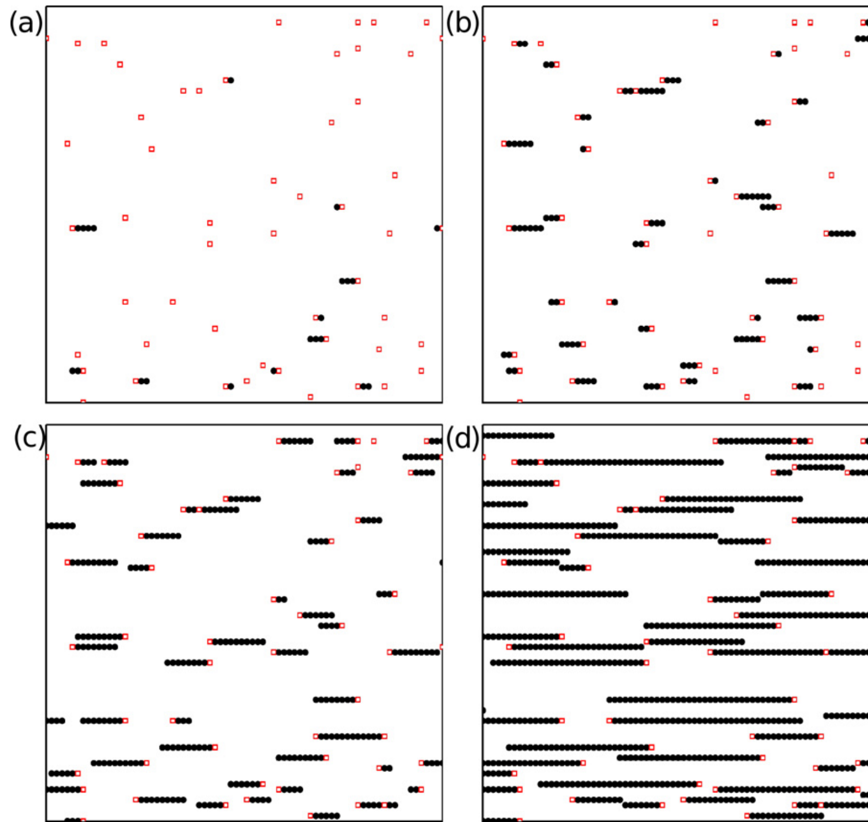

Figure 2. Simulated room-temperature surface morphology of In chains grown on Si(100) at various coverages (a) 0.005 ML, (b) 0.02 ML, (c) 0.05 ML, and (d) 0.15 ML. C-defect density is 0.01/site. Constituent atoms within islands appear as filled black circles; defects appear as unfilled red circles and can be seen terminating islands.

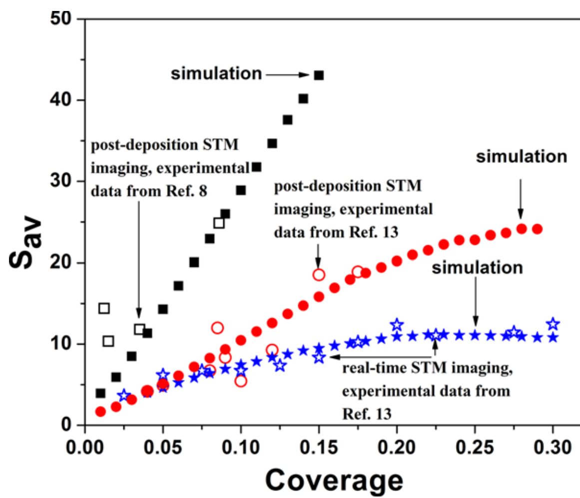

Figure 3. Simulated mean island size versus coverage for three different experimental conditions using post-deposition and real-time STM imaging techniques. Unlike in post-deposition imaging, the C-defect density for the latter case is not fixed but increases during the course of the experiment (and simulation). The corresponding experimental data from [8, 13] are included for comparison.

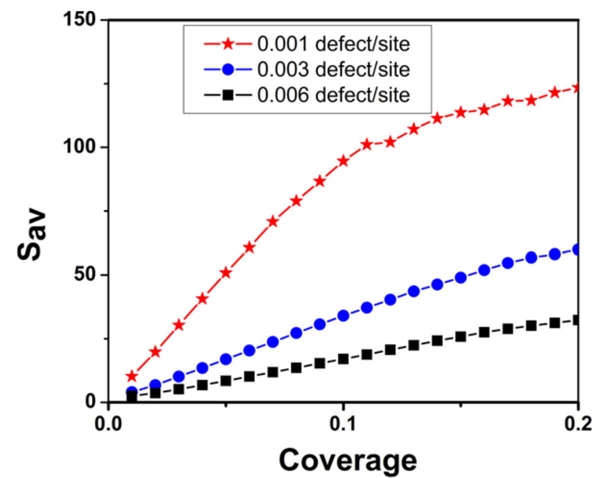

Figure 4. Simulated mean island size versus coverage for different values of the defect density, with $F = 2 \times 10^{-3}$ ML s^{-1}.

the experiment and setting the defect density to a slightly higher value (0.0035/site) in the simulations, we are able to fit simulation data with experimental results starting at 0.04 ML. Notice that the dip evident in the experimental data at low coverages (<0.04 ML) is not replicated in the simulations. However, this feature was not easily explained and, in fact, was not observed in a similar experimental study detailed in [13].

Next, we performed additional simulations corresponding to real-time STM imaging data presented in [13] (unfilled blue stars) obtained during deposition with low flux, $F = 10^{-4}$ ML s^{-1}. As described in section 3.2, the C-defect density continues to increase throughout the duration of the real-time

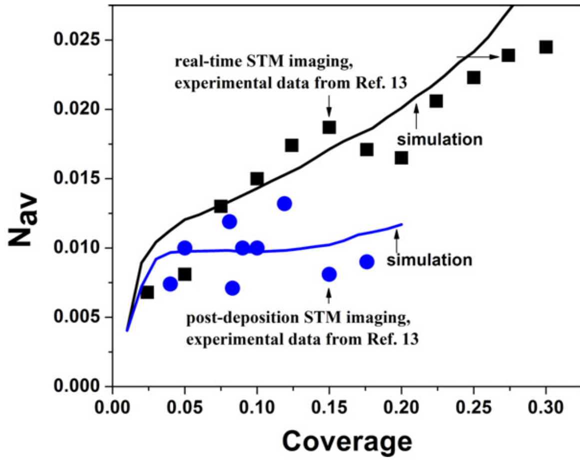

Figure 5. Mean island density versus coverage. Simulation results are compared with selected experimental data. In the simulations, an initial C-defect density of 0.01/site was assumed for both real-time and post-deposition imaging, a value deduced from figure 2 in [13].

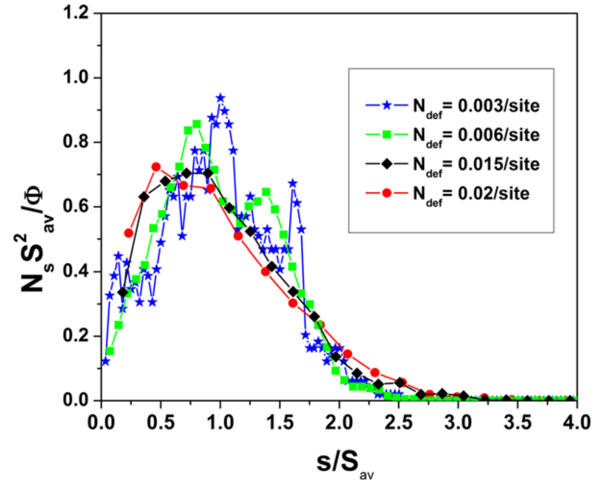

Figure 6. Scaled ISD for various C-defect densities, with $F = 2 \times 10^{-3}$ ML s^{-1}. The figure shows a clear trend towards monotonically decreasing ISD as C-defect densities are increased.

imaging experiment from some initial value. We assume that this initial C-defect density is the same as the (roughly constant) value of 0.01/site determined in the post-deposition imaging experiment. The (experimental) rate at which the C-defect increases with time, $\sim 10^{-6}$ ML s^{-1}, can be deduced from figure 2 in [13]. Thus, in the simulations (filled blue stars), we start with an initial defect density of 0.01/site, then add C-defects as the simulation progresses. We found that adding defects at the rate of 4.5×10^{-6} ML s^{-1} results in a reasonably good fit with experiment. The flatter curve corresponds to more persistent nucleation due to the continual introduction of defect sites.

As complementary representation of behavior, in figure 5 we compare simulation results for the mean island density $N_{\rm av} = \theta/S_{\rm av}$, in both the above types of experiments with their experimental counterparts in [13]. In the simulation, an initial defect density of 0.01/site has been assumed. The most striking difference between the fast and slow deposition results (both experiment and simulation) is the roughly constant island density in the former which is in sharp contrast with the quasi-linearly increasing behavior of the latter. As discussed in [13], this follows from the fact that defects act as nucleation sites. Specifically, an increasing (constant) defect density induces the quasi-linearly increasing (nearly constant) island density in the slow (fast) deposition studies.

4.3. Shape of island size distribution

The scaled island size distribution (ISD), f, is defined so that the density of islands or chains of size s satisfies $N_s \propto f(s/S_{\rm av})$. Choosing a normalization constant of $N_{\rm av}/S_{\rm av} = S_{\rm av}^2/\theta$ ensures that $\int f(x)\,{\rm d}x = \int x f(x)\,{\rm d}x = 1$ [24]. Simulation results are shown in figure 6 where the defect density (which is constant during the simulation run) ranges from a fixed low value of 0.003/site to around 0.02/site. The scaled ISD progressively deviates from a monomodal form (which is the default expectation for both homogeneous and heterogeneous nucleation [24]) towards a monotonically decreasing form as the defect density is increased. For a defect density of 0.02/site, typical of the experimental studies detailed in [13], the shape of the ISD is closer to a monotonically decreasing form rather than a monomodal form.

Our prediction for the shape of the ISD has been confirmed experimentally in the same study, which reported a monotonically decreasing ISD for In in experiments with low flux and real-time imaging during deposition where defect density is expected to exceed 0.02/site. In previous work [9], we argued that inhibited aggregation relative to homogeneous island nucleation can produce monotonically decreasing island size distribution. (Inhibited aggregation boosts the population of diffusing adatoms and thus facilitates persistent homogeneous nucleation.) In the current modeling, homogeneous nucleation is not significant, and the large ratio of diffusion to deposition rates ensures that monomers are rare. (See section 4.4 for further discussion.) Here, instead, a key factor is the density of defects: more defects allow more nucleation of new islands which helps a shift towards a monotonically decreasing distribution. This effect is evident in figure 6, where we plot the ISD for several values of the defect density. Increasing the defect density leads progressively to a more monotonically decreasing ISD.

It is clear that once defects become saturated, island growth rates will simply reflect the areas of the Voronoi cells associated with the defect distribution. For lower defect densities, where saturation is achieved quickly, the monomodal island size distribution reflects the monomodal Voronoi cell distribution [25]. By contrast, with high defect density the late stage saturated growth is never reached and the ISD takes a different form.

4.4. Homogeneous versus heterogeneous nucleation

The relative degree of homogeneous versus heterogeneous nucleation is naturally controlled by the relative magnitude of the defect separation, $L_{\rm def}$, and a suitably defined diffusion length, $L_{\rm diff}$. The former is directly obtained from the defect

density via $L_{\rm def} = N_{\rm def}^{-1/2}$. The latter corresponds to the mean island separation for purely homogeneous nucleation, which is a non-trivial quantity. If $L_{\rm diff} \gg L_{\rm def}$ ($L_{\rm diff} \ll L_{\rm def}$), then heterogeneous (homogeneous) nucleation dominates [27]. Since the mean island separation for homogeneous nucleation decreases with increasing terrace diffusion rates, it is clear that heterogeneous nucleation will dominate for high terrace diffusion rates or high defect densities. It should, however, be noted that the dependence of the island density on diffusion rates and barriers is distinct for isotropic and anisotropic diffusion [24]. The former results should be used for our system.

Another key factor is the strength of the adatom attractions, as weak interactions lead to reversible island formation with much lower island densities and much higher island separations [24]. Thus, in this regime, heterogeneous nucleation would dominate. Applying the above analysis of the In/Si(100) system for the parameters used in our modeling makes clear that heterogeneous nucleation should dominate (due to rapid terrace diffusion, weak adatom interactions, and high defect densities).

Next, we apply the above ideas to elucidate the contrasting behavior for Ga/Si(100) and In/Si(100) [10]. Although heterogeneous nucleation of atomic chains is significant during room-temperature deposition of Ga on Si(100) [4, 9], it is not dominant. Stronger Ga–Ga attractions (relative to In–In) were suggested to play a role. To clarify this issue, we have performed simulations for Ga deposition with the model described in this paper but suitably adjusting the parameters. In our simulation runs, we used a flux rate, $F = 10^{-3}$ ML s^{-1} and defect density, $N_{\rm def} = 0.003$/site to reflect actual experimental conditions. For the surface diffusion barriers, the values $E_{\perp,\parallel} = 0.4(0.81)$ eV which we previously predicted in [9] were used. To mimic stronger attractions for Ga, we decrease detachment rates from chains of even length by a factor of around 48 (corresponding at 300 K to an increase in the barrier of 0.1 eV). Our results indicate that the ratio of homogeneous to heterogeneously nucleated islands at 0.04 ML is around 19, an order of magnitude higher than the experimental value $\sim$1.42 [10][8]. This suggests an overestimation of the surface diffusion barriers in our previous study. This discrepancy notwithstanding, we have established that a confluence of factors including lower defect density ($\sim$0.003/site), lower terrace diffusivity [9], and strong adatom attractions [7] shift the system (relative to In) to favor homogeneous nucleation.

Finally, it was questioned in [26] whether the introduction of heterogeneous nucleation in the modeling of Ga deposition on Si(100) would produce the observed monotonically decreasing size distribution. The result of simulations using the parameters above and a defect density of 0.003 ML s^{-1} is shown in figure 7 confirming that the ISD remains monotonically decreasing in the presence of both types of nucleation pathway. The key factor producing such an ISD, persistent nucleation, results from two factors. On the one hand, high densities of diffusing adatoms even at a relatively high coverage due to restriction aggregation facilitates continued homogeneous nucleation. On the other hand, the presence of many islands (boosted by the number of homogeneous islands) which act as sinks for diffusing atoms presumably slows the saturation of C-defects by heterogeneously nucleated islands, opening another pathway for persistent nucleation.

[8] Quantifying homogeneous versus heterogeneous nucleation is complicated by the fact that certain islands appear to nucleate at or near defects other than C-type (i.e. missing dimers, trimers, etc). Of the 63 nucleation events tracked in [10], 16 appeared to have nucleated by non-type C-defects.

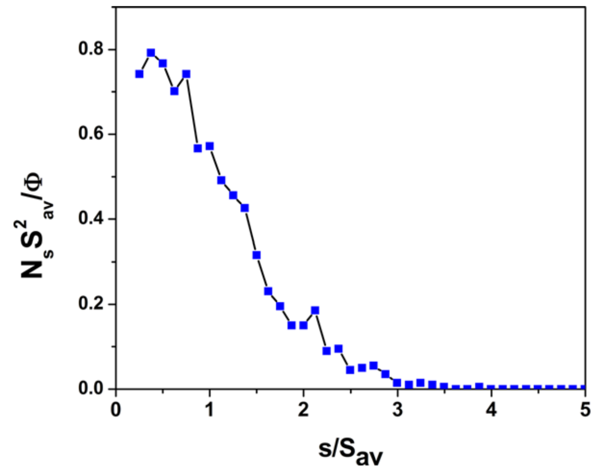

Figure 7. Simulated scaled ISD for the Ga/Si(100) system. In this simulation, $F = 2 \times 10^{-3}$ ML s^{-1}, $(E_\perp, E_\parallel) = (0.4$ eV, 0.81 eV), while defect density is set to 0.003/site. The shape of distribution is arguably monotonically decreasing.

5. Conclusions

We have developed a lattice-gas model for deposition of In atoms on Si(100) surfaces guided by recent experimental observations regarding the dominance of island nucleation at C-type defects and also the reversibility of island formation. We show that this model with realistic rate parameters suggested from our own DFT calculations as well as from real-time STM observations can describe experimental observations on mean island size and density, as well as the island size distribution. Specifically, we were able to demonstrate that a monotonically decreasing island size distribution is consistent with high defect density, and that a low defect density leads to early saturation of defects with islands, resulting in a linear increase in mean island size with time. Finally, we have elucidated the conditions controlling the dominance of heterogeneous versus homogeneous nucleation in these systems.

Acknowledgments

This work was supported by the NCTS and the National Science Council of Taiwan under grant No. NSC95-2112-M110-022. We are grateful to the National Center for High-performance Computing in Taiwan for computer time and facilities. JWE was supported by the US Department of Energy (USDOE), Office of Basic Energy Sciences through the Division of Chemical Sciences. His work was performed at the

Ames Laboratory which is operated for the USDOE by Iowa State University under contract No. DE-AC02-07CH11358.

References

[1] Nogami J, Baski A A and Quate C F 1991 *Phys. Rev.* B **44** 1415
[2] Baski A A, Nogami J and Quate C F 1991 *Phys. Rev.* B **43** 9316
[3] Dong Z, Yakabe T, Fujita D, Jiang Q and Nejo H 1997 *Surf. Sci.* **380** 23
[4] Nogami J and Evans M M R 1999 *Surf. Rev. Lett.* **6** 1067
[5] Brocks G, Kelly P J and Car R 1993 *Phys. Rev. Lett.* **70** 2786
[6] Dai X Q, Ju W W, Wang G T and Xie M H 2004 *Surf. Sci.* **572** 77
[7] Takeuchi N 2000 *Phys. Rev.* B **63** 035311
[8] Nogami J 1997 *Atomic and Molecular Wires* (*NATO ASI Series E: Applied Sciences* vol 341) ed C Joachim and S Roth (Dordrecht: Kluwer) p 11
[9] Albao M A, Evans M M R, Nogami J, Zorn D, Gordon M S and Evans J W 2005 *Phys. Rev.* B **72** 035426
[10] Albao M A, Evans M M R, Nogami J, Zorn D, Gordon M S and Evans J W 2006 *Phys. Rev.* B **74** 037402
[11] Zorn D D, Albao M A, Evans J W and Gordon M S 2009 *J. Phys. Chem.* C **113** 7277
[12] Kocan P, Sobotik P, Ostadal I, Javorsky J and Setvin M 2007 *Surf. Sci.* **601** 4506
[13] Ostadal I, Javorsky J, Kocan P, Sobotik P, Ostadal I and Setvin M 2008 *J. Phys.: Conf. Ser.* **100** 072006
[14] Kocan P, Jurczyszyn L, Sobotik P and Ostadal I 2008 *Phys. Rev.* B **77** 113301
[15] Javorsky J, Setvin M, Ostadal I, Sobotik P and Kotrla M 2008 *WDS'08 Proc. of Contributed Papers, Part III* vol 95
[16] Chan T L, Wang C Z, Lu Z Y and Ho K M 2005 *Phys. Rev.* B **72** 045405
[17] Perdew J P, Burke K and Ernzerhof M 1996 *Phys. Rev. Lett.* **77** 3865
[18] Hohenberg P and Kohn W 1964 *Phys. Rev.* **136** B864
Kohn W and Sham L J 1965 *Phys. Rev.* **140** A1135
[19] Kresse G and Joubert D 1999 *Phys. Rev.* B **59** 1758
[20] Kresse G and Hafner J 1993 *Phys. Rev.* B **47** 558
Kresse G and Furthmüller J 1996 *Phys. Rev.* B **54** 11169
[21] Chuang F C 2007 *Phys. Rev.* B **75** 115408
[22] Chan T L, Ye Y Y, Wang C Z and Ho K M 2006 *Surf. Sci.* **600** L159
[23] Bortz A B, Kalos M H and Lebowitz J L 1975 *J. Comput. Phys.* **17** 10
[24] Evans J W, Thiel P A and Bartelt M C 2006 *Surf. Sci. Rep.* **61** 1
[25] Mulheran P A and Blackman J A 1995 *Phil. Mag. Lett.* **72** 55
[26] Kocan P, Sobotik P and Ostadal I 2006 *Phys. Rev.* B **74** 037401
[27] Vardavas R, Ratsch C and Caflisch R E 2004 *Surf. Sci.* **569** 185